Supporting Information

Inhibiting cathode dissolution and shuttling of V-O species by a polybenzimidazole hydrogel electrolyte for durable high-areal-capacity Zn-V_2O_5 batteries

*Zeheng Lv,[a] Rong Tang,[a] Chenxi Sun,[a] Weiwei Meng,[b] Jin Yang,[a] Siyang Li,[a] Qilong Wu,[a] Minghao Zhang,[a] Jinbao Zhao,[*a] Yang Yang [*a]*

[a]State Key Laboratory of Physical Chemistry of Solid Surfaces, State-Province Joint Engineering Laboratory of Power Source Technology for New Energy Vehicle, College of Chemistry and Chemical Engineering, Xiamen University, Xiamen, 361005, P. R. China

[b]Key Laboratory of Functional Materials and Devices for Special Environments of CAS, Xinjiang Key Laboratory of Electronic Information Materials and Devices; Xinjiang Technical Institute of Physics & Chemistry of CAS, Urumqi 830011, P. R. China

AUTHOR INFORMATION

Corresponding Author

*E-mail: jbzhao@xmu.edu.cn; yangyang419@xmu.edu.cn

Experimental Section

Preparation of PBI hydrogel electrolyte

1 g PBI (polybenzimidazole) powder was dissolved in 9 g DMAC (N, N-dimethylacetamide, Aladdin, 99.0%) solvent with magnetic stirring at 95 °C for at least 12 h to get a homogeneous casting solution. Then the casting solution was taken to cool down to room temperature naturally, and cast on a clean and dust-free glass substrate with a blade. After that, the above glass substrate was soaked in deionized water for phase inversion at least 48 h. Subsequently, the PBI hydrogel membrane peeled off the glass substrate, and was washed and stored in deionized water. Finally, the PBI hydrogel membrane was immersed in 3 M $Zn(OTF)_2$ at least 48 h to prepared the PBI hydrogel electrolyte.

The PBI hydrogel electrolyte containing the other components can be obtained through the same above procedure.

Preparation of $V_2O_5 \cdot 1.6\ H_2O$

The $V_2O_5 \cdot 1.6\ H_2O$ was synthesized via the previous reported hydrothermal method with a moderated modification.[1, 2] 0.33 g V_2O_5 (Macklin, >99%), 60 mL deionized water and 1.5 mL 30% H_2O_2 (Xilong Science, AR) were mixed with magnetic stirring for 30 min. Then the mixture was transferred to an 80 mL Teflon autoclave and maintained at 190 °C for 6 h. After cooling down to room temperature, the resultant was dried by vacuum freeze drying at least 72 h to obtain the product.

Preparation of V_2O_5 and $V_2O_5 \cdot 1.6\ H_2O$ cathodes

V_2O_5/$V_2O_5 \cdot 1.6\ H_2O$, carbon black and PVDF (polyvinylidene fluoride) at a weight

ratio of 7:2:1 in NMP (N-methyl-2-pyrrolidone) solvent were mixed to form the even slurries with magnetic stirring, then the slurries were coated onto hydrophilic conductive carbon cloth or stainless steel, and dried using a vacuum oven at 80 °C overnight. The final loading mass of V_2O_5 on carbon cloth and stainless steel were 4.8-5.5 and 3.0-4.5 mg cm^{-2}, respectively, and the loading mass of $V_2O_5 \cdot 1.6\ H_2O$ on carbon cloth and stainless steel were 2.5-3.0 and 5.0-5.5 mg cm^{-2}, respectively.

Wherein, the electrodes using carbon cloth current collectors were utilized for electrochemical cycling tests, and the electrodes using stainless steel current collectors were utilized for in-situ XRD measurements.

Assembly and electrochemical measurements of Zn||Zn symmetrical batteries

The bare Zn, cathode electrode, GF (glass fiber) separator and PBI hydrogel membrane were pressed and punched out into circular disks. The diameters of Zn metal and cathode electrode were 12 mm (~ 1 cm^2), and the diameters of GF separator and PBI hydrogel membrane were 19 mm. Before battery fabrication, the free liquid electrolyte on the surface of PBI hydrogel were carefully removed by air-laid paper.

The bare Zn as both working and counter electrodes, couple with the PBI hydrogel electrolyte or liquid electrolytes, were assembled into symmetrical Zn||Zn cells. For DEMS measurements, the Zn||Zn cells were cycling at a current density of 10 mA cm^{-2} with a capacity of 5 mAh cm^{-2}.

Assembly and electrochemical measurements of full cells

The full cells were assembled with the as-prepared V_2O_5/$V_2O_5 \cdot 1.6\ H_2O$ cathodes, liquid 3 M Zn $(OTF)_2$ (120 μL) or PBI hydrogel electrolytes containing 3 M Zn$(OTF)_2$ (two

piece of the thin PBI electrolytes, the thickness of one PBI electrolyte in the battery is ~ 100 μm, the water content in PBI electrolyte is about 30.9%), and bare Zn metal anode in CR2032 coin cells in an open atmosphere. The thickness of a stainless steel spacer is 1 mm. The full cells were galvanostatic charging-discharging between 0.2 and 1.6 V at 0.1, 0.2 or 1 A g^{-1}. All full cells were tested on a Neware battery system.

Before the normal electrochemical cycling tests, the pristine commercial V_2O_5 cathodes need to experience the pre-activation cycling processes firstly. The pre-activation procedures were set to be as follow: cycling at 0.1 A g^{-1} for three cycles and then cycling at 1 A g^{-1} until the charge capacity of V_2O_5 cathode reaches over 350 mAh g^{-1} (a larger cycling rate is adopted to reduce the pre-activation time). When the pre-activation processes were finished, the dissembled V_2O_5 cathodes and cathodic electrolyte were coupled with the fresh Zn metal anode and anodic electrolyte to reconstruct the Zn||V_2O_5 batteries. To reach the initial stable state, the Zn||V_2O_5 batteries should be activated at 0.2 or 1 A g^{-1} for one cycle before long-term electrochemical cycling at 0.2 or 1 A g^{-1}.

Quantitative measurements of ionic conductivities of PBI hydrogel electrolyte

PBI hydrogel electrolyte containing 3 M $Zn(OTF)_2$ was sandwiched between two stainless steel spacers to measure EIS (100 kHz to 0.01 Hz). Ionic conductivities (σ) were calculated according to the following equation:

$$\sigma = \frac{l}{RS}$$

where R represents the resistance according to EIS measurement, l represents the thickness of PBI hydrogel membrane, and S is the area of PBI hydrogel electrolyte.

Characterizations

Field emission scanning electron microscope (FESEM) measurements were conducted on Zeiss GeminiSEM 500. X-ray diffraction (XRD) patterns were collected through X Malvern Panalytical (Empyrean) with Cu Kα radiation (λ =1.5406 Å). Raman spectra were tested via LabRAM HR Evolution (HORIBA FRANCE) using irradiation source with 532 nm laser. Fourier transform infrared (FT-IR) spectra and ATR were analyzed by a Bruker Vertex 70V FT-IR spectrometer. Inductively coupled plasma-optical emission spectrometry (ICP-OES, SPECTRO SPECTROBLUE FMX36) was applied to analyze the content of V^{5+}. The ^{51}V nuclear magnetic resonance (NMR) spectroscopy of the V-O species saturated solution (immersing excessive V_2O_5 powder into 3 M $Zn(OTF)_2$ for more than two months) was collected on a 500 MHz NMR spectrometer (Bruker AVANCE NEO 500). And the deuterated reagent utilized for NMR test was D_2O (deuterium oxide). The linear sweep voltammetry (LSV,) tests were conducted in a three-electrode system from -1.05 V to -1.8 V at 5 mV s^{-1} by the electrochemical workstation (CHI 660E, chinstruments). The bare Zn and PBI-Zn (the Zn metal was coated with PBI hydrogel for testing), platinum plate, and Ag/AgCl were employed as the work, counter and reference electrodes, respectively, and the 1 M Na_2SO_4 aqueous solution was selected as supporting electrolyte to avoid the influence of zinc electrodepositing.

The in-situ XRD measurement and the galvanostatic charging and discharging were performed in the in-situ electrochemical XRD battery. The batteries were fabricated by V_2O_5/V_2O_5·1.6 H_2O cathodes, liquid 3 M Zn $(OTF)_2$ and PBI hydrogel electrolytes

containing 3 M $Zn(OTF)_2$, and bare Zn metal anode. Every single XRD pattern was collected by X Malvern Panalytical (Empyrean) with the X-ray radiation wavelength of 1.5406 Å (Cu Kα).

The in-situ differential electrochemical mass spectroscopy (DEMS, HPR-40, R&D) was performed to monitor the hydrogen evolution rate in Zn||Zn symmetrical batteries with liquid 3 M Zn $(OTF)_2$ and PBI hydrogel electrolytes.

The in-situ electrochemical quartz crystal microbalance (EQCM) test results were obtained by QSense Explorer (Biolin Scientific) and its electrochemistry module (QEM 401). The Au circular 5 MHz AT-cut quartz substrates with an active area of 0.785 cm^{-2} (QSX 301 Au) were used to measure the mass and dissipation factor changes of the electrode. To characterize the effect of suppressing V_2O_5 dissolution, the V_2O_5 powder was mixed with PVDF and PBI binders at a weight ratio of 9:1 in NMP and DMAC solvents, respectively. After ultrasonic treatment on the above mixtures for 30 min, a little of the resultants were cast on QSX 301 Au. 3 M $Zn(OTF)_2$, Pt electrode, and Ag/AgCl were employed as the electrolyte, counter electrode and reference electrode, respectively. The electrochemical workstation (CHI 440B, chinstruments) was utilized to carry out the cyclic voltammetry control. The potential scan region was ± 0.6 V (vs. Ag/AgCl) with the scan rates of 0.5 and 5 mV s^{-1}. According to the Sauerbrey equation, the mass change was calculated as $\Delta m = -C \times \Delta f / n$. The C is the sensitivity constant, which is 17.7 ng Hz^{-1} cm^{-2} here. The n is the odd multiple of frequency, thus the n=1 for base frequency and n=3 for triple frequency (f3). In this work, the f3 was employed as the excitation frequency, thus the 1 Hz increase in frequency correspond to a mass

decrease of 4.63 ng.

Theoretical calculations

Quantum chemistry (QC) calculation was performed with Gaussian09 E.01[3] software in this work. The B3LYP-D3[4, 5] functional and def2-SVP[6] basis set was used to optimize the geometry of all structures. The vibration analysis was performed at the same theoretical level to ensure that all structures to be energy minima and get Gibbs free energy correction. The high-precision single-point energy was calculated by Gaussian09 E.01 at the B3LYP-D3/def2-TZVPP[6, 7] theoretical level. Solvent effects of water (ε = 78.4) were considered by SMD[8] solvation model. The electrostatic potential (ESP) was calculated through Multiwfn[9, 10] software.

The DFT calculations were carried out using the Vienna Ab initio Simulation Package (VASP)[11]. The core electrons were modeled with the projector-augmented-wave (PAW) method[12]. The exchange and correlation functional of Perdew-Burke-Ernzerhof (PBE) was adopted within the framework of generalized gradient approximation (GGA)[13]. The plane-wave basis cut-off energy was set to 500 eV. The structures were relaxed until the forces and total energy on all atoms were converged to less than 0.02 eV Å and 1×10^{-5} eV, respectively. Visualization of the structures is made by using VESTA software. To explore the interactions between H_2O and substrates V_2O_5(110) cleaved from the corresponding crystal structure, a vacuum layer of 20 Å was adopted. The differential charge density was calculated according $\Delta\rho = \rho_{12} - \rho_1 - \rho_2$, where ρ_1, ρ_{12} and ρ_2 are the charge density of H_2O, V_2O_5(110) with and without water adsorbed on the surface, respectively. Yellow and blue colors indicate the charge accumulation

and depletion, respectively. 2D Slice of the differential charge density is made by VESTA software.

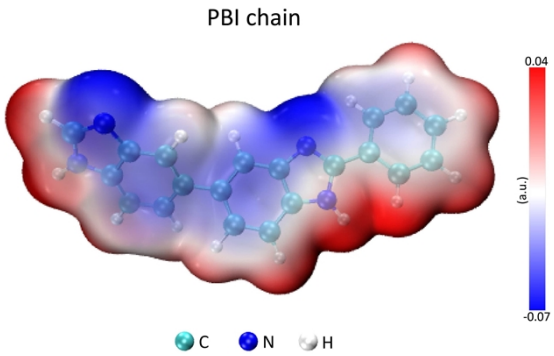

Fig. S1 ESP result of PBI chain.

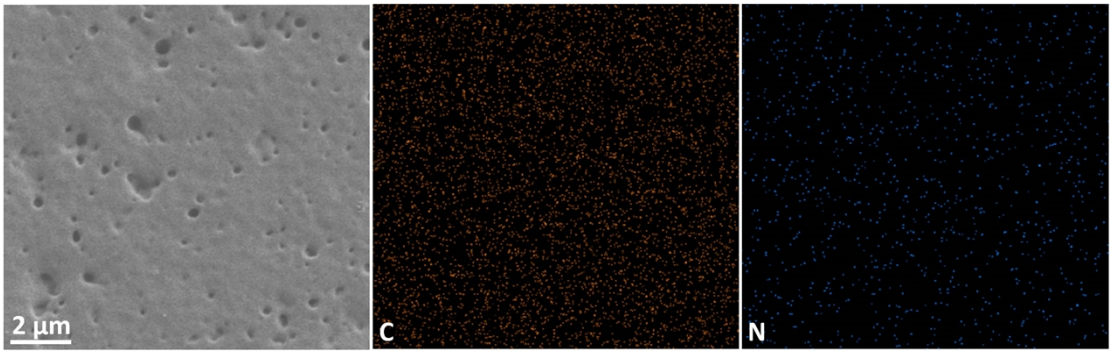

Fig. S2 SEM image and the corresponding C/N elemental mappings of PBI membrane.

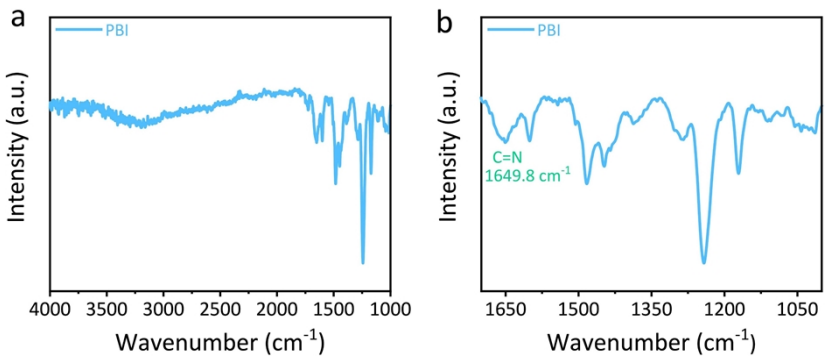

Fig. S3 FT-IR spectra of the PBI membrane at the range of (a) 4000-1000 cm^{-1} and (b) 1700-1000 cm^{-1}.

The FT-IR spectra of the PBI membrane is consistent with the previous reported results, and the characteristic peak at ~ 1649.8 cm^{-1} can be attributed to the pyridine N of C=N groups.[14-17]

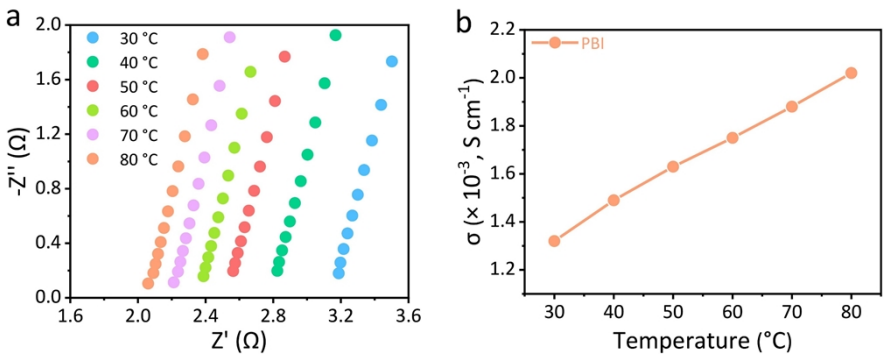

Fig. S4 (a) EIS results of PBI hydrogel electrolyte at various temperatures. (b) Ionic conductivities of PBI hydrogel electrolyte at various temperatures.

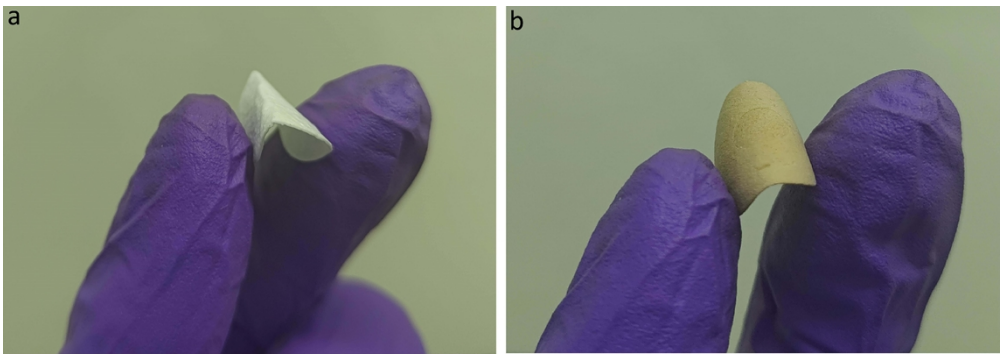

Fig. S5 The flexibility comparison of the (a) conventional used GF separator and (b) PBI membrane.

The above results indicates that the flexibility of PBI membrane can be comparable to that of the conventional used GF separator.

Fig. S6 Thickness measurement of the PBI electrolyte.

The above result shows that the thickness of the PBI electrolyte is around 150-160 µm. Besides, the PBI electrolyte can be further compressed in batteries, and the thickness can be as thin as below 100 µm.

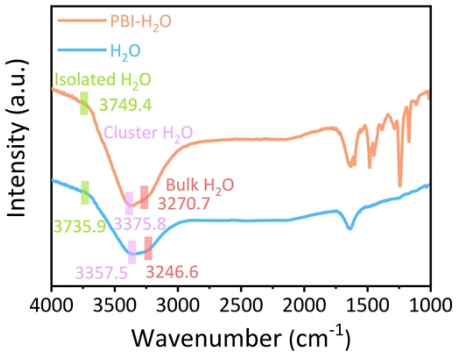

Fig. S7 FT-IR spectra of the PBI-H_2O and H_2O at the range of 4000-1000 cm^{-1}.

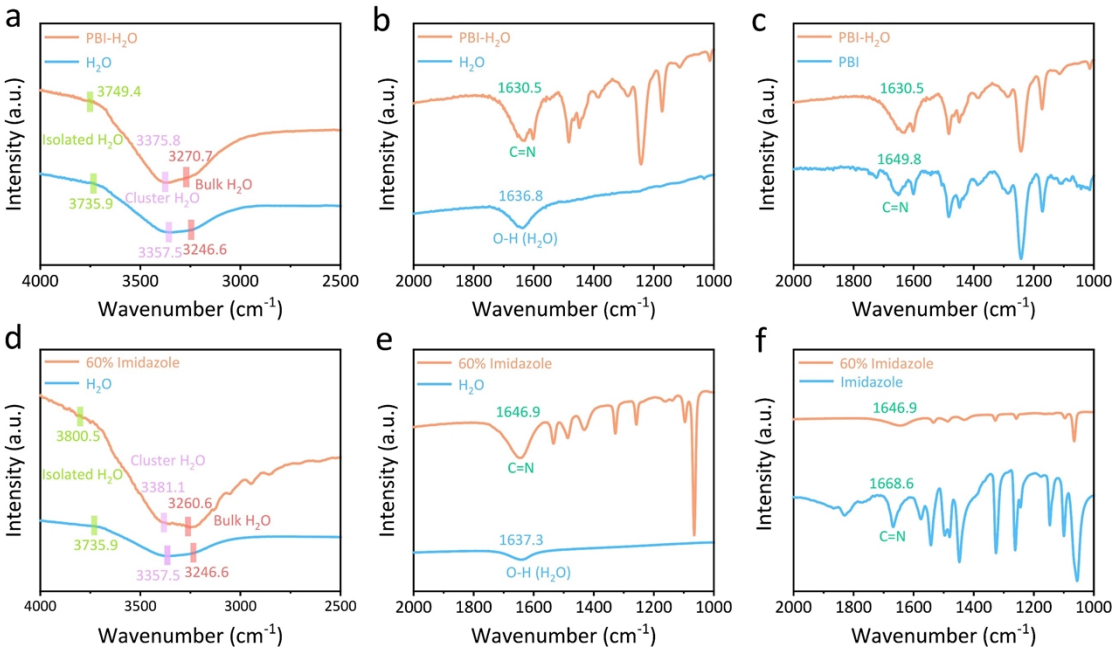

Fig. S8 FT-IR spectra of the (a, b) PBI-H_2O and H_2O, (c) PBI-H_2O and PBI, (d, e) 60% imidazole and H_2O, and (f) 60% imidazole and the pure imidazole.

The O-H stretching vibration of water molecules usually appears as a broad FT-IR band around 3200-3800 cm^{-1} (Fig. S8a), and blue shifts in the O-H stretching mode are often attributed to interactions between water molecules and the other polar groups.[18] And the characteristic broad peaks of water would transform into the relatively narrow ones after interacting with external polar groups. Along with the blue shift in the O-H stretching mode, the O-H bending mode of water molecules at ~ 1637 cm^{-1} (Fig. S8b) also shifts to a higher wavenumber. However, the simultaneous changes in the C=N and O-H in PBI-H_2O cause these two peaks merging into one (Fig. S8b). The altered peak at ~ 1630.5 cm^{-1} can therefore be assigned to the C=N group of PBI (Fig. S8c).

Considering the molecular structural similarity between imidazole and PBI

monomer (Fig. S9), the interaction between imidazole and water was also investigating using FT-IR. In Fig. S8d, the blue shifts of O-H stretching mode are also observed in 60% imidazole (the mass fraction of imidazole in aqueous solution is 60 wt%), accompanied by the disappearance of O-H bending mode and the red shift of C=N characteristic peak (Fig. S8e and f), suggesting the potential interaction between the pyridine N of imidazole ring and water molecules.

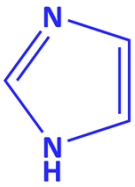

Fig. S9 Molecular structure of the imidazole.

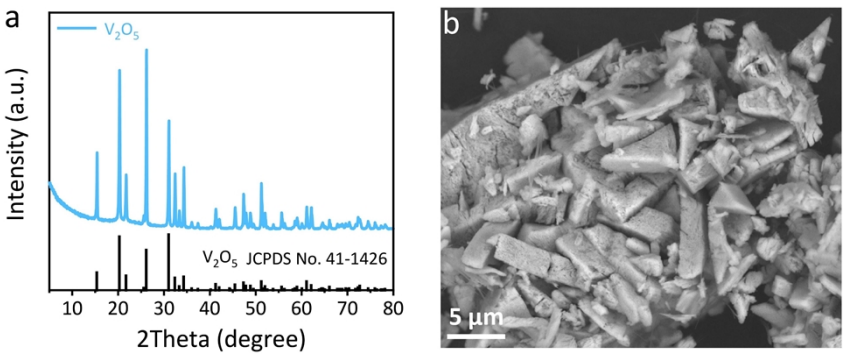

Fig. S10 (a) XRD result of the commercial V_2O_5 powder. (b) SEM image of the commercial V_2O_5 powder.

The commercial anhydrous V_2O_5 was employed as a typical case to study the influence of water activity on the cycling stability of Zn-V_2O_5 battery. The initial irregular bulk morphology of the V_2O_5 powder was reported previously.[19]

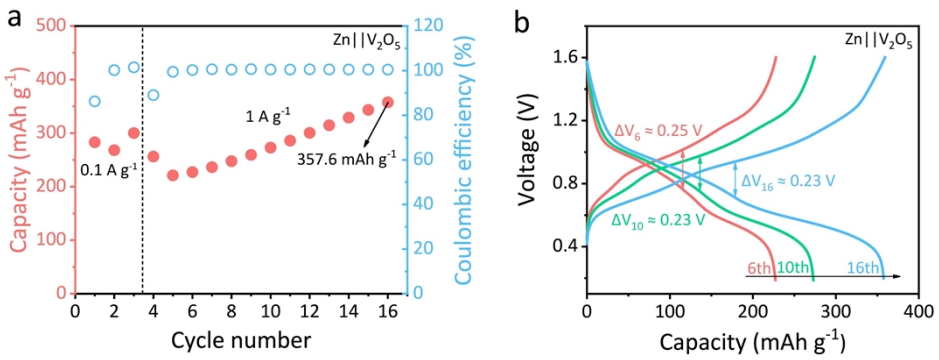

Fig. S11 (a) Typical customized sequential activation procedures and (b) the corresponding discharge-charge curves for Zn||V_2O_5 batteries.

Before the normal electrochemical cycling tests, the pristine commercial V_2O_5 cathodes need to experience the pre-activation cycling processes firstly. The pre-activation procedures were set to be as following: cycling at 0.1 A g^{-1} (0.2 C) for three cycles and then cycling at 1 A g^{-1} (1.7 C) until the charge capacity of V_2O_5 cathode reaches over 350 mAh g^{-1} (a larger cycling rate is adopted to reduce the pre-activation time). During the activation process, the capacity of V_2O_5 is increasing along with the polarization decrease.

When the pre-activation processes were finished, the dissembled V_2O_5 cathodes and cathodic electrolyte were coupled with the fresh Zn metal anode and anodic electrolyte to reconstruct the Zn||V_2O_5 batteries. To reach the initial stable state, the Zn||V_2O_5 batteries should be activated at 0.2 (0.3 C) or 1 A g^{-1} (1.7 C) for one cycle before long-term electrochemical cycling at 0.3 or 1.7 C.

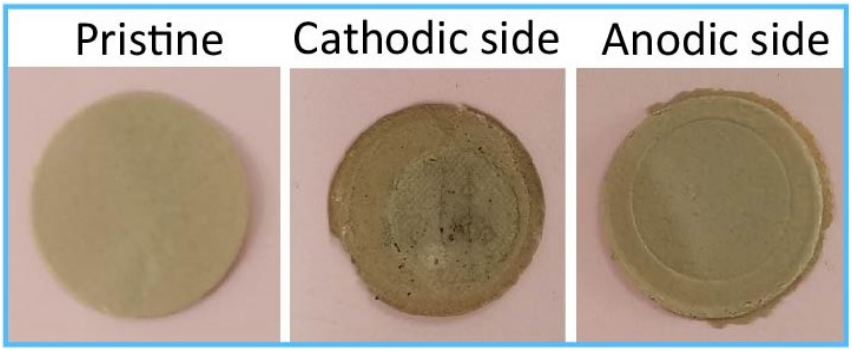

Fig. S12 PBI separators before and after pre-activation.

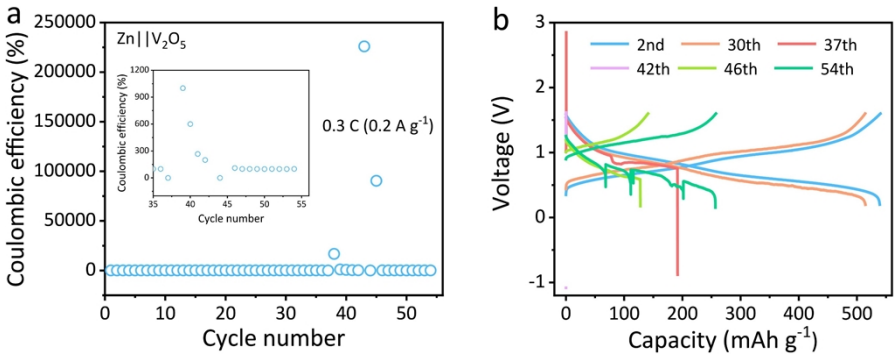

Fig. S13 (a) Coulombic efficiencies of Zn||V_2O_5 battery with 3 M $Zn(OTF)_2$ at 0.3 C. (b) The corresponding discharge-charge curves for Zn||V_2O_5 battery with 3 M $Zn(OTF)_2$ at 0.3 C.

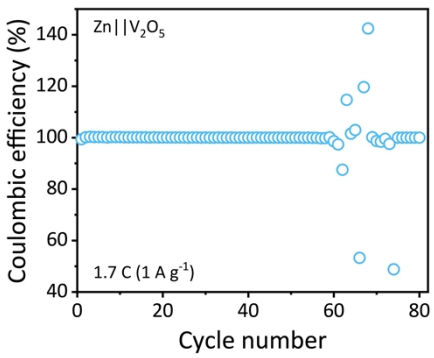

Fig. S14 Coulombic efficiencies of Zn||V_2O_5 battery with 3 M $Zn(OTF)_2$ at 1.7 C.

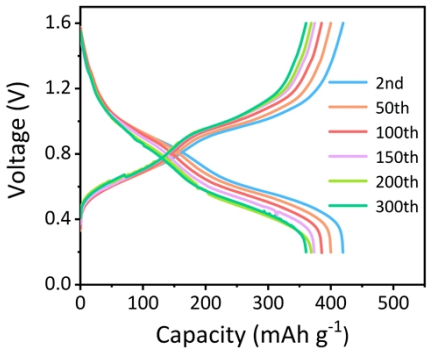

Fig. S15 The discharge-charge curves for Zn||V_2O_5 battery with PBI hydrogel electrolyte at 0.3 C.

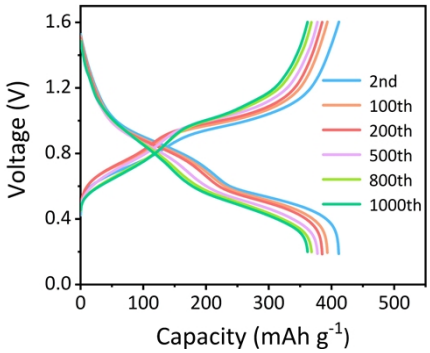

Fig. S16 The discharge-charge curves for Zn||V_2O_5 battery with PBI hydrogel electrolyte at 1.7 C.

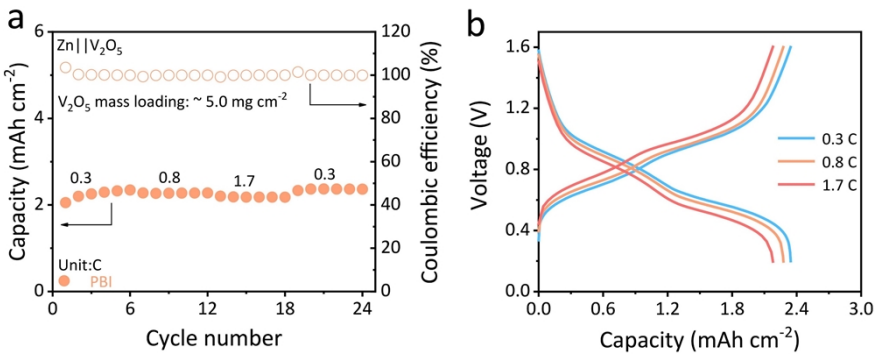

Fig. S17 (a) Rate capability of Zn||V_2O_5 battery with PBI hydrogel electrolyte. (b) The corresponding discharge-charge curves for Zn||V_2O_5 battery with PBI hydrogel electrolyte.

After a pre-activation, the V_2O_5 cathode can show a good rate capability, which is consistent with previous report.[19] It can be inferred that the pre-activation process that increasing the interlayer spacing of V_2O_5 may be effective in enhancing electrochemical kinetics of V_2O_5 cathodes. In addition, after a pre-activation, the charge transfer resistance of V_2O_5 cathode shows a significant decrease (Fig. S18), and the redox reactions of V_2O_5 cathode also exhibit a good reversibility at different scan rates (Fig. S19), thereby contributing to the good rate capability for V_2O_5 cathode. Moreover, to examine the maximum rate the battery can offer, the rate capability of V_2O_5 cathode at the larger rates was further tested. As shown in Fig. S20, when the rate is increased to > 8.5 C, the battery shows both huge electrochemical polarization and obvious capacity decay, therefore, the maximum rate the battery can offer could be determined to be as ~ 8 C.

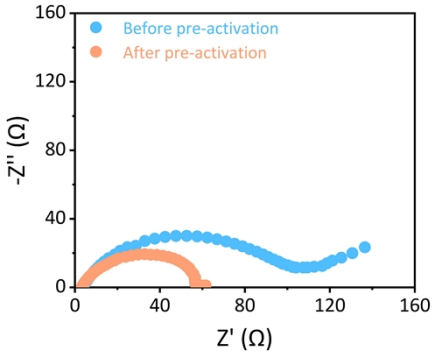

Fig. S18 EIS results of Zn||V_2O_5 battery with PBI hydrogel electrolyte before and after pre-activation.

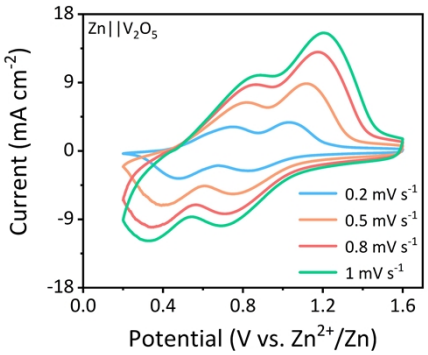

Fig. S19 CV results of Zn||V_2O_5 battery with PBI hydrogel electrolyte after pre-activation.

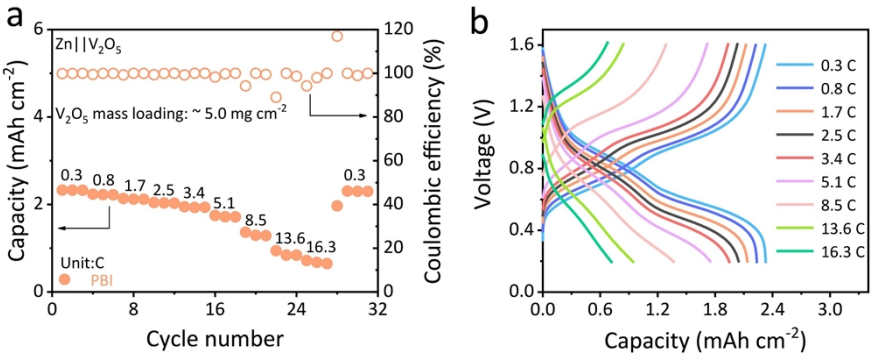

Fig. S20 (a) Rate capability of Zn||V_2O_5 battery with PBI hydrogel electrolyte at the larger rates. (b) The corresponding discharge-charge curves for Zn||V_2O_5 battery with PBI hydrogel electrolyte.

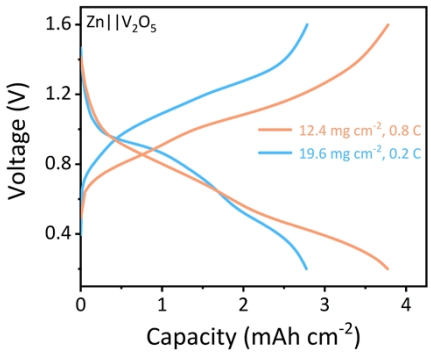

Fig. S21 Estimation of areal capacity limit for Zn||V_2O_5 pouch cell with PBI hydrogel electrolyte.

The V_2O_5 loading was increased beyond 10 mg cm^{-2} to evaluate the capacity limit using PBI electrolytes in practical pouch cells. As shown in Fig. S21, as the loading mass of V_2O_5 cathodes is increased to 12.4 mg cm^{-2}, the areal capacity of Zn||V_2O_5 pouch cell reaches as high as ~ 4 mAh cm^{-2} at 0.8 C. However, when the loading mass is further increased to 19.6 mg cm^{-2}, the areal capacity does not increase as expected and instead decrease to only ~ 2.9 mAh cm^{-2} at 0.2 C. This super-high loading Zn||V_2O_5 pouch cell exhibits significant electrochemical polarization, implying that the electrode fabricating method requires careful optimization to ensure efficient electron and ion transport in such a high-loading cathode. In addition, the important study had revealed that as the loading mass of active materials increase, the ion migration resistance and the charge transfer resistance in the electrode will also increase because of the increased diffusion lengths for ion/electron.[20] According to the reported method, the V_2O_5||V_2O_5 symmetric cells were fabricated for EIS measurement. As shown in Fig. S22, when the loading mass of V_2O_5 was increased to ~ 19 mg cm^{-2}, the internal resistance of cell (R_c) shows a significant increase, indicating

the super-high loading mass would easily lead to the higher contact resistance between V_2O_5 cathode and electrolyte, and block the ion migration from electrolyte to V_2O_5 cathode. Moreover, the electron conductivity resistances (R_e) of these V_2O_5 cathodes were also measured (Fig. S23). The thicknesses of the V_2O_5 cathodes with ~ 5, 12 and 19 mg cm^{-2} are ~ 370, 482 and 576 μm, respectively, and the resistance in Fig. S23 for the V_2O_5 cathodes with ~ 5, 12 and 19 mg cm^{-2} are 0.9, 1.1 and 2.7 Ω, respectively, reflecting the decreased electron conductivity of the V_2O_5 cathodes with ~ 19 mg cm^{-2}. Therefore, for the V_2O_5 cathode with super-high loading mass, the larger R_c and R_e are likely to block both ion migration and electron transfer processes in the bulk of the V_2O_5 electrode (Fig. S24), which would potentially result in the lower capacity utilization of the V_2O_5 electrode. In the future research, the slow kinetics of mass and charge transfer processes in the thick electrode should be noted, and the improved strategies may could focus on improving the tap density and electron conductivity of the active material, and enhancing the ion migration rate in the whole electrode through adding the ion conductive agent and employing the more effective pre-activation method.

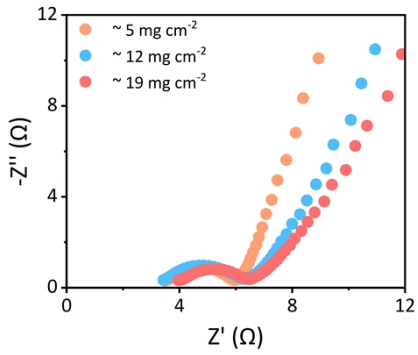

Fig. S22 Nyquist plots depending on the loading mass of the V_2O_5 cathode.

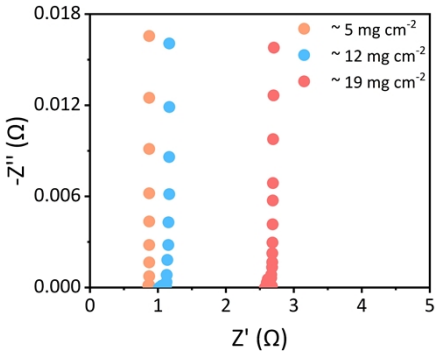

Fig. S23 EIS results of the V_2O_5 cathode with different loading mass. V_2O_5 cathode was sandwiched between two stainless steel spacers to measure EIS.

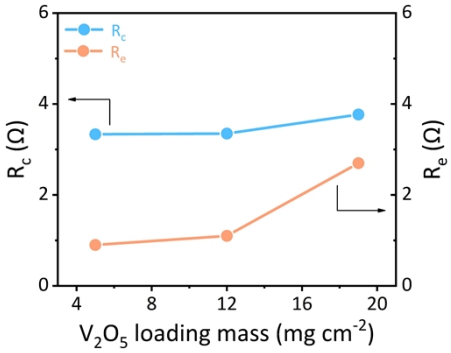

Fig. S24 R_c and R_e depending on the V_2O_5 loading mass.

Overall, the areal capacity limit of Zn||V_2O_5 pouch cell using PBI electrolytes, based on the conventional slurry-coating cathode fabrication method, is estimated to be approximately 4 mAh cm^{-2}. The cycling performances of Zn||V_2O_5 pouch cell and coin cell at 1.7 C were also tested (Fig. S25 and S26). The pouch cell and coin cell can cycle with ~ 4 mAh cm-2 for 25 and 50 cycles, respectively, demonstrating the practicality of the PBI electrolyte in Zn-V_2O_5 batteries.

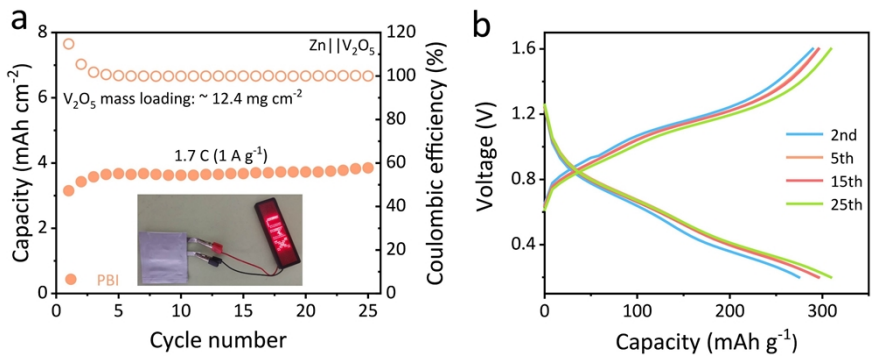

Fig. S25 (a) Cycling performance of Zn||V_2O_5 pouch cell with PBI hydrogel electrolyte at 1.7 C, and (b) the corresponding charge-discharge profiles. The inset in Fig. S25a is the Zn||V_2O_5 pouch cell lighting the LED panel, and the carbon cloth with V_2O_5 is bound on the titanium foil with a thickness of 50 μm to improve the mechanical strength of the external cathode tab.

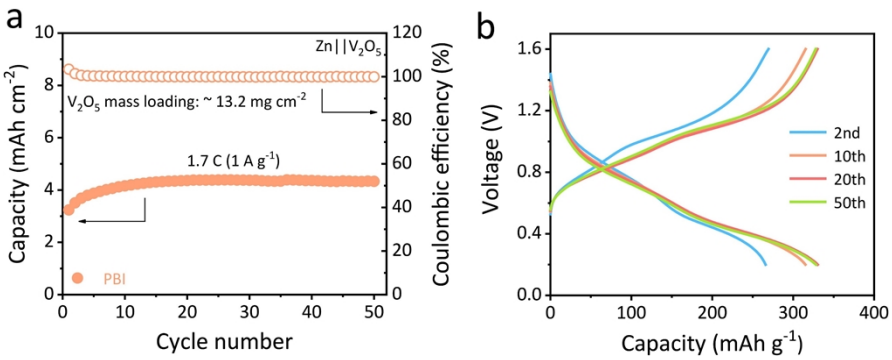

Fig. S26 (a) Cycling performance of Zn||V_2O_5 coin cell with PBI hydrogel electrolyte at 1.7 C, and (b) the corresponding charge-discharge profiles.

Table S1. The comparison of low-rate (＜2 C) cycling stabilities between Zn||V_2O_5 coin cells using PBI hydrogel electrolyte and the other reported V-based materials.

Cathode	Mass loading (mg cm^{-2})	Current (A g^{-1})	Capacity (mAh cm^{-2})	Cycle number	Reference
VOH	1-2	0.5	0.5	200	[21]
ZVO	1-2	0.5	0.7	200	[21]
V_2O_5	4.5	0.5	0.7	1000	[22]
PEO-LVO	2	0.5	0.7	100	[23]
$VOOH/VS_x$	1.8-2.3	0.5	0.7	120	[24]
		1	0.7	180	
MIL-88B(V)@rGO	1.0-1.5	2	0.4	400	[25]
NVO	1.5	0.2	0.3	100	[26]
ZVO	3.75	0.15	0.5	350	[27]
	42.46	0.045	4.4	250	
NVO	6.6	0.5	0.9	3000	[28]
CaVO	3.2	1	0.9	2000	[29]
MnVO	1-2	0.2	0.4	100	[30]
		0.5	0.4	200	
V_2O_5	5.0	0.2	2.0	300	This work
		1	1.7	1000	

The capacities are calculated based on the final reversible capacities and the highest mass loading of active materials.

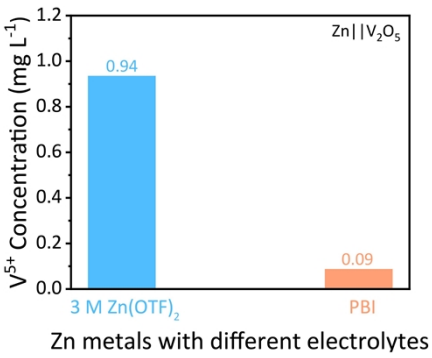

Fig. S27 The ICP results of the V^{5+} content for the dissembled Zn metals after 10 cycles at 0.2 C in Zn||V_2O_5 batteries.

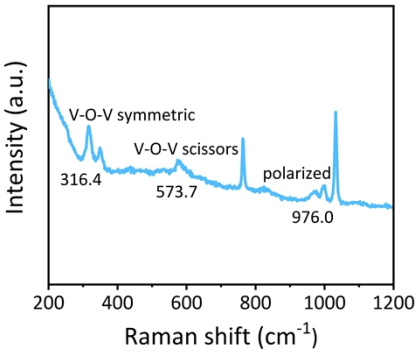

Fig. S28 Raman result of the as-prepared $V_{10}O_{26}(OH)_2^{4-}$ aqueous solution.

0.9-1 g V_2O_5 powder was completely dissolved in aqueous 6 M KOH solution, and then the pH was adjusted to ~ 3.34 (the pH of 3 M $Zn(OTF)_2$ was ~ 3.23) via trifluoromethanesulfonic acid (CF_3SO_3H). Through ICP measurement, the V^{5+} concentration of the as-prepared V-O aqueous solution was 1.46 g L^{-1} (0.03 mol L^{-1}), indicating the V-O species may be $V_{10}O_{26}(OH)_2^{4-}$ possibly.[31] According to the Raman result, three characteristic peaks at 316.4, 573.7 and 976.0 cm^{-1} could be attributed to V-O-V symmetric, V-O-V scissors and polarized vibration modes of the $V_{10}O_{26}(OH)_2^{4-}$.[32] Therefore, the V-O species in the as-prepared aqueous solution can be recognized as the $V_{10}O_{26}(OH)_2^{4-}$.

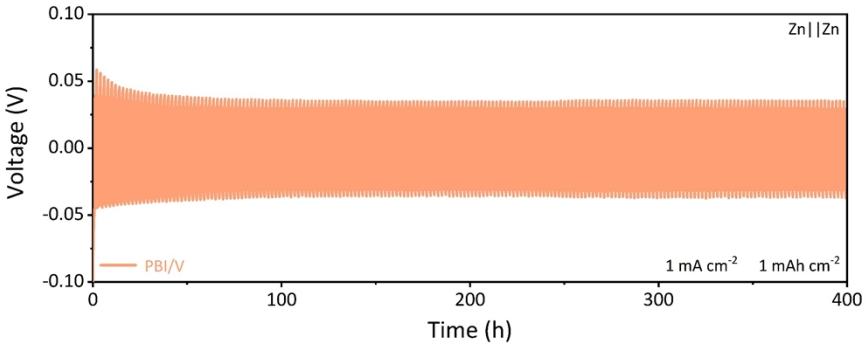

Fig. S29 Cycling performance of Zn||Zn battery with 1 mA cm^{-2} and 1 mAh cm^{-2}.

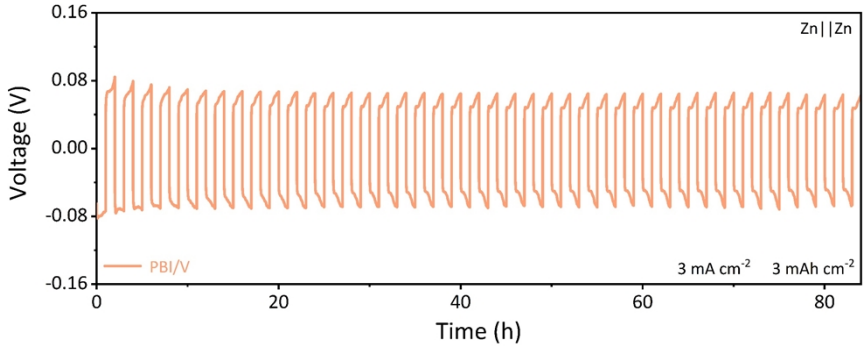

Fig. S30 Cycling performance of Zn||Zn battery with 3 mA cm^{-2} and 3 mAh cm^{-2}.

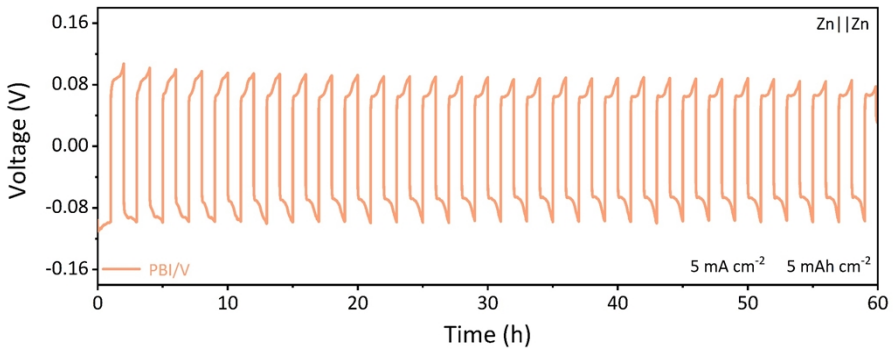

Fig. S31 Cycling performance of Zn||Zn battery with 5 mA cm^{-2} and 5 mAh cm^{-2}.

The Zn||Zn symmetrical cell can cycle stably with PBI/V for about 400 h at an areal capacity of 1 mAh cm^{-2} (Fig. S29). Moreover, the Zn||Zn symmetrical cell also can cycle at the higher areal capacity (Fig. S30 and S31), demonstrating the PBI can stabilize the

V-O species and suppress the V^{5+} deposition onto the Zn metal.

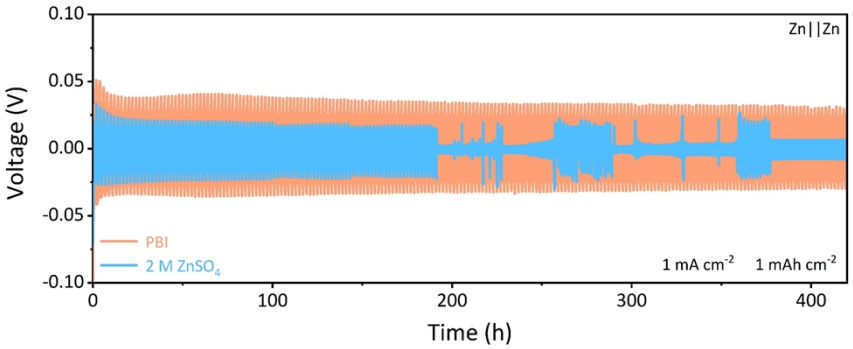

Fig. S32 Cycling performance of Zn||Zn batteries with 1 mA cm^{-2} and 1 mAh cm^{-2}.

The Zn||Zn symmetrical cell can cycle stably with PBI over 400 h, illustrating the PBI can also improve the reversibility of Zn metal anode in the commonly employed electrolyte of 2 M $ZnSO_4$.

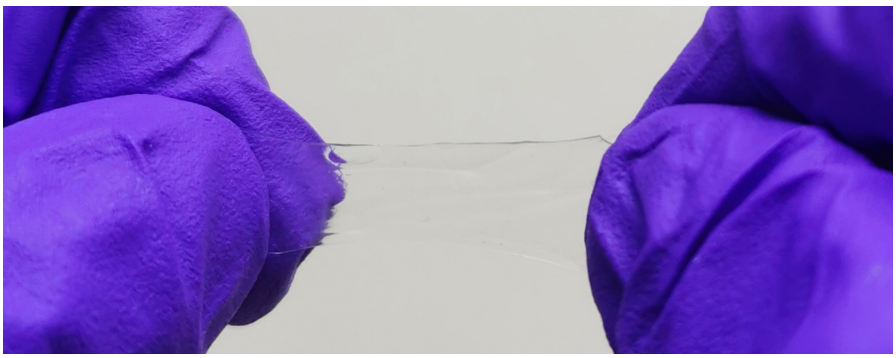

Fig. S33 The photo of the PAM hydrogel.

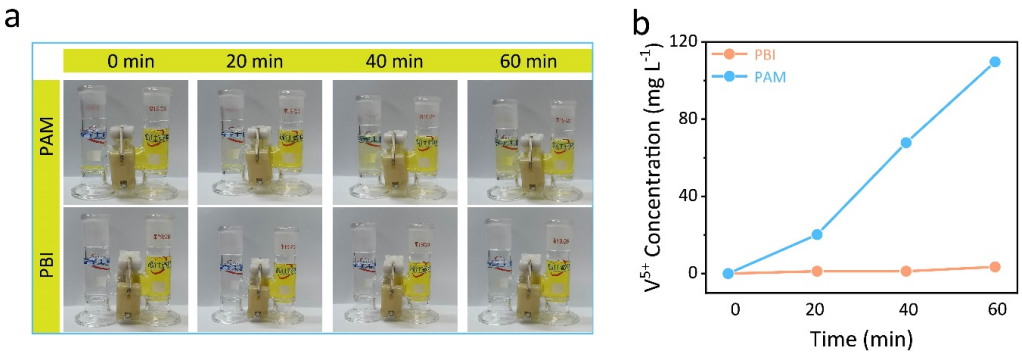

Fig. S34 (a) Visual penetration processes of the freshly prepared V-O solution (the V^{5+} concentration was 0.23 g L^{-1}), and (b) the corresponding ICP results for PAM and PBI hydrogels.

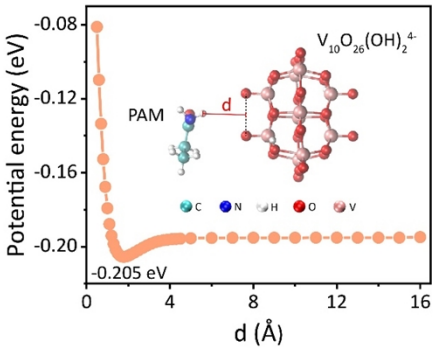

Fig. S35 Evolution of potential energies with different distances between PAM and $V_{10}O_{26}(OH)_2^{4-}$.

As many other hydrogel electrolytes (or the so-called two-in-one electrolytes) also possess the functions of physical barriers and chemical adsorption effect, and the typical polyacrylamide (PAM) hydrogel electrolyte is often believed that the functional polar acyl group could adsorb Zn^{2+} ions with a significant negative binding energy, so that the PAM can act as an intermediate to transport Zn^{2+} ions uniformly from electrolyte to the surface of Zn anode by the abundant zinc-oriented acyl group on the polymer.[33-36] However, the effect on blocking the shuttling of V-O species for PAM hydrogel is insufficient to be understood.

Herein, through the free-radical polymerization approach,[37] the cross-linked PAM hydrogel was prepared (Fig. S33). The results of the $V_{10}O_{26}(OH)_2^{4-}$ solution penetration experiment in Fig. S34 reflect that the PBI can be more effective in suppressing the $V_{10}O_{26}(OH)_2^{4-}$ shuttling while compared with the PAM hydrogel. However, through the ESP simulation (Fig. S35), it can be found that the negative $V_{10}O_{26}(OH)_2^{4-}$ would bind with the positive -NH- group of PAM and the binding energy is as high as -0.205 eV, suggesting the potential adsorption interaction between PAM and $V_{10}O_{26}(OH)_2^{4-}$. The inferior practical anti-penetration effect of PAM on $V_{10}O_{26}(OH)_2^{4-}$ could be speculated as the highly water-soluble acrylamide precursor cause the resulted PAM hydrogel show high compatibility with water, so that the V-O species would easily move with water molecules through PAM hydrogel. We speculate that the effective strategy of improving the practicality of PAM could focus on adjusting the composition and preparing the multilayer structure of PAM hydrogel. Therefore, the PBI electrolyte could effectively reduce the water activity and stabilize the dissolved V-O species, so

that both V_2O_5 dissolution and the crosstalk of V-O species between V_2O_5 cathode and Zn anode could be suppressed. Besides, an ideal two-in-one electrolyte for prolonging the lifespan of Zn-V_2O_5 batteries should at least possess the specific features including (1) reducing water activity in electrolyte, and (2) suppressing the V-O species shuttling.

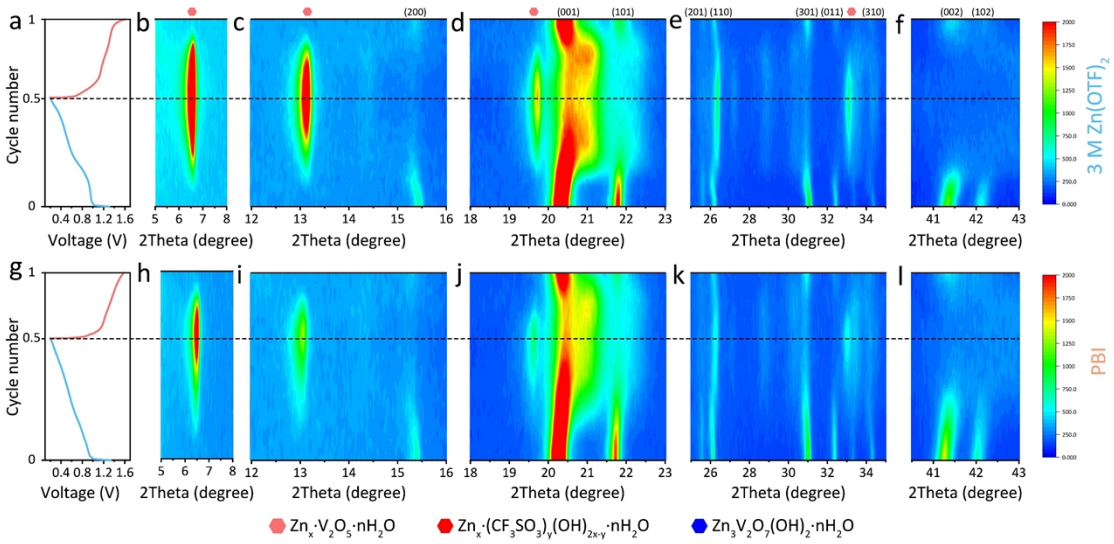

Fig. S36 Discharge-charge curves of Zn||V_2O_5 batteries with (a) 3 M $Zn(OTF)_2$ and (g) PBI hydrogel electrolytes during the initial cycle. The corresponding in-situ XRD results of Zn||V_2O_5 batteries with (b-f) 3 M $Zn(OTF)_2$ and (h-l) PBI hydrogel electrolytes.

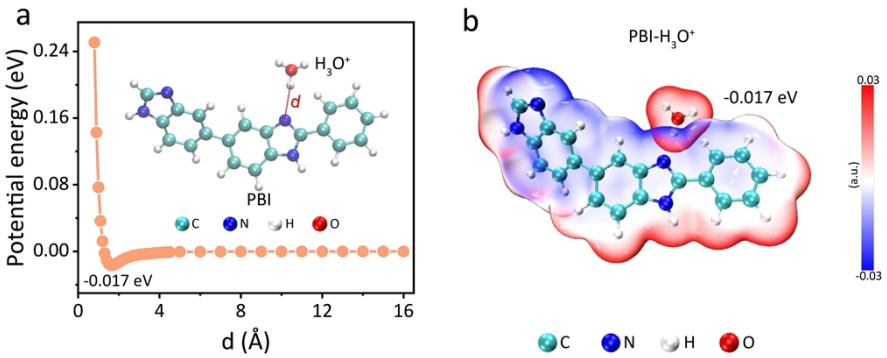

Fig. S37 (a) Evolution of potential energies with different distances between PBI and H_3O^+. (b) ESP result of PBI-H_3O^+.

The lower binding energy of -0.017 eV between H_3O^+ and PBI indicates the solvated water could substantially screen the electrostatic interaction (Fig. S37), so that the dominant form of proton for electrochemical intercalation may be H_3O^+, particularly in PBI electrolytes. And the free H^+ also would be restricted by PBI chain, so that the PBI electrolyte should help to inhibit proton insertion into the V_2O_5 host.

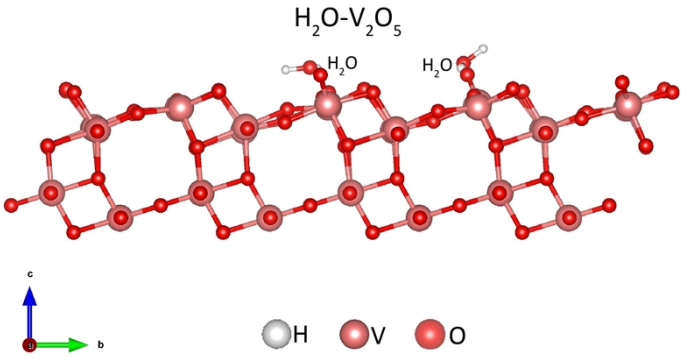

Fig. S38 Static interaction between H_2O and V_2O_5.

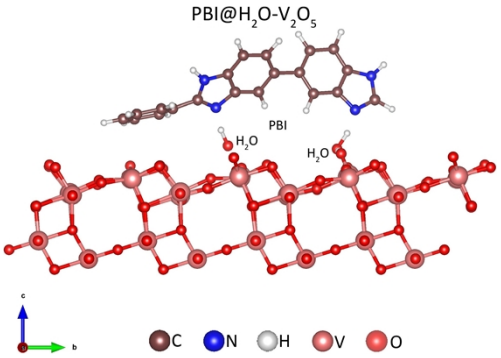

Fig. S39 Static interaction between PBI@H_2O and V_2O_5.

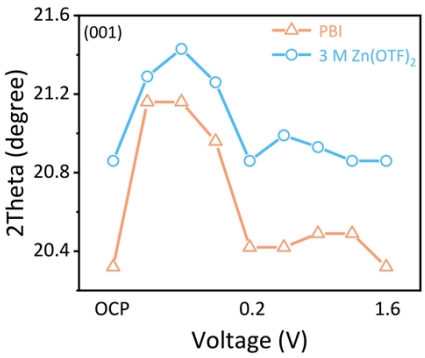

Fig. S40 (001) peak evolutions of hydrated V_2O_5 cathodes with 3 M $Zn(OTF)_2$ and PBI hydrogel electrolytes. The selective states with 3 M $Zn(OTF)_2$ are OCP (open circuit potential), 0.7, 0.6, 0.5, 0.2, 0.9, 1.0, 1.2 and 1.6 V, and OCP, 0.8, 0.6, 0.5, 0.2, 0.7, 0.9, 1.1 and 1.6 V with PBI.

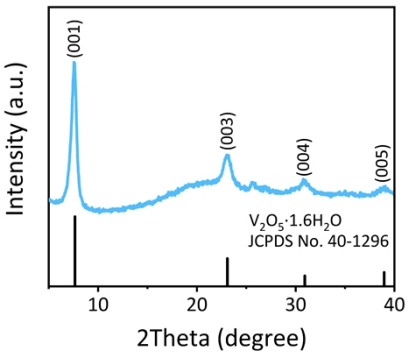

Fig. S41 XRD result of the $V_2O_5 \cdot 1.6H_2O$ powder.

The $V_2O_5 \cdot 1.6H_2O$ is formed by pre-inserting water molecules into the interlayer space of V_2O_5 without other impurities, so the inconspicuous peak at ~ 26° can be assigned to pristine V_2O_5 host.[1] And the changeable position of the (001) peak is relevant to the synthesized condition, the amount of interlayer water molecules, and the ambient humidity possibly.

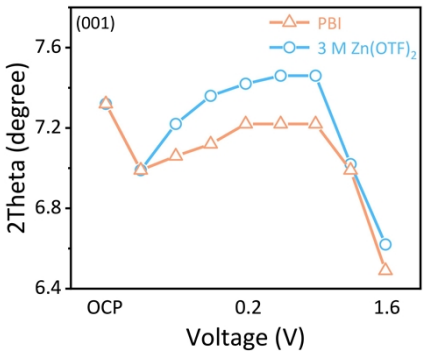

Fig. S42 (001) peak evolutions of $V_2O_5 \cdot 1.6H_2O$ cathodes with 3 M $Zn(OTF)_2$ and PBI hydrogel electrolytes. The selective states with 3 M $Zn(OTF)_2$ are OCP, 0.9, 0.7, 0.6, 0.2, 1.0, 1.1, 1.3 and 1.6 V, and OCP, 0.9, 0.7, 0.5, 0.2, 0.9, 1.0, 1.2 and 1.6 V with PBI.

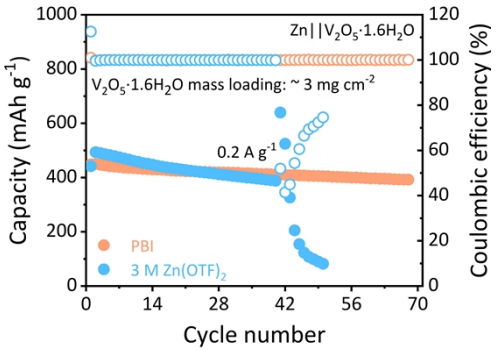

Fig. S43 Cycling performances of Zn||V_2O_5·1.6H_2O batteries with 3 M $Zn(OTF)_2$ and PBI hydrogel electrolytes at 0.2 A g^{-1}.

The higher cycling stability of Zn||V_2O_5·1.6H_2O battery using PBI electrolyte further verify the roles of PBI in inhibiting V_2O_5 dissolution and promoting $[Zn(H_2O)_x]^{2+}$ intercalation.

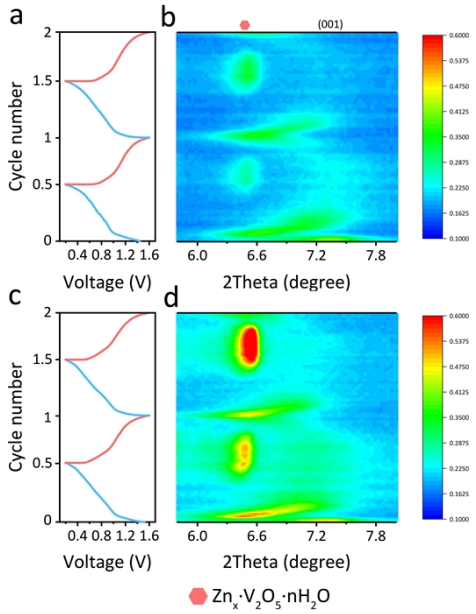

Fig. S44 Discharge-charge curves of the $V_2O_5 \cdot 1.6H_2O$ cathodes with (a) 3 M $Zn(OTF)_2$ and (c) PBI hydrogel electrolytes during the initial two cycles. The corresponding normalized in-situ XRD results with (b) 3 M $Zn(OTF)_2$ and (d) PBI hydrogel electrolytes.

It is noticed that the position of (001) peak in $V_2O_5 \cdot 1.6H_2O$ cathode shifts to a lower degree after the initial cycle, which could be attributed to that the irreversible residual interlayer water and Zn^{2+} ions cause the interlayer spaces of $V_2O_5 \cdot 1.6H_2O$ to be larger than the pristine state. Afterward, the $V_2O_5 \cdot 1.6H_2O$ with larger interlayer space shows a reversible evolution of (001) peak during the 2nd cycle, indicating the enlarged interlayer distance may be beneficial for subsequent ion intercalation.

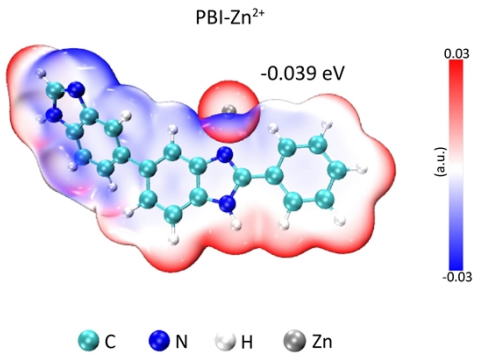

Fig. S45 ESP result of PBI-Zn^{2+}.

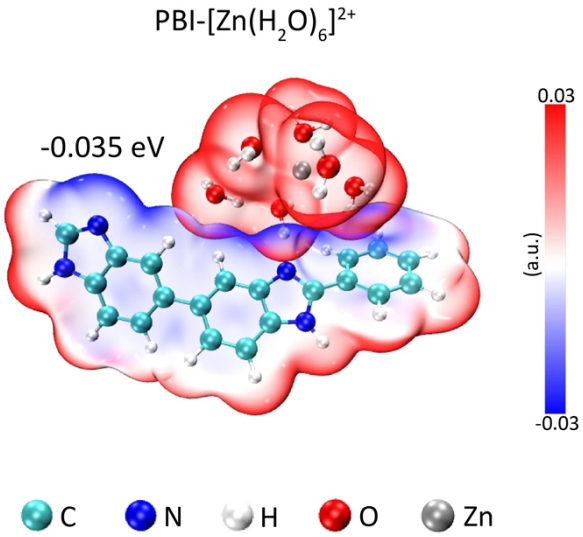

Fig. S46 ESP result of PBI-$[Zn(H_2O)_6]^{2+}$.

Reference

1. X. Wang, L. Ma, P. Zhang, H. Wang, S. Li, S. Ji, Z. Wen and J. Sun, *Appl. Surf. Sci.*, 2020, **502**, 144207.

2. P. Lin, J. Cong, J. Li, M. Zhang, P. Lai, J. Zeng, Y. Yang and J. Zhao, *Energy Storage Mater.*, 2022, **49**, 172-180.

3. M. J. Frisch, G. W. Trucks, H. B. Schlegel, G. E. Scuseria, M. A. Robb, J. R. Cheeseman, G. Scalmani, V. Barone, B. Mennucci, G. A. Petersson, H. Nakatsuji, M. Caricato, X. Li, H. P. Hratchian, A. F. Izmaylov, J. Bloino, G. Zheng, J. L. Sonnenberg, M. Hada, M. Ehara, K. Toyota, R. Fukuda, J. Hasegawa, M. Ishida, T. Nakajima, Y. Honda, O. Kitao, H. Nakai, T. Vreven, J. A. Montgomery, Jr, J. E. Peralta, F. Ogliaro, M. Bearpark, J. J. Heyd, E. Brothers, K. N. Kudin, V. N. Staroverov, R. Kobayashi, J. Normand, K. Raghavachari, V. N. Staroverov, R. Kobayashi, J. Normand, K. Raghavachari, A. Rendell, J. C. Burant, S. S. Iyengar, J. Tomasi, M. Cossi, N. Rega, N. J. Millam, M. Klene, J. E. Knox, J. B. Cross, V. Bakken, C. Adamo, J. Jaramillo, R. Gomperts, R. E. Stratmann, O. Yazyev, A. J. Austin, R. Cammi, C. Pomelli, J. W. Ochterski, R. L. Martin, K. Morokuma, V. G. Zakrzewski, G. A. Voth, P. Salvador, J. J. Dannenberg, S. Dapprich, A. D. Daniels, Ö. Farkas, J. Foresman, J. V. B.; Ortiz, J. Cioslowski, D. J. Fox, Gaussian 09, Revision E.01, Gaussian, Inc., Wallingford CT, 2013.

4. Stephens, P. J., Devlin, F. J., Chabalowski, C. F., Frisch and M. J., *J. Phys. Chem.*, 1994, **98**, 11624-11627.

5. S. Grimme, J. Antony, S. Ehrlich and H. Krieg, *J. Phys. Chem.*, 2010, **132**, 154104.

DOI: 10.1063/1.3382344.

6. F. Weigend and R. Ahlrichs, *Phys. Chem. Chem. Phys.*, 2005, **7**, 3297-3305. DOI: 10.1039/b508541a.

7. F. Weigend, *Phys. Chem. Chem. Phys.*, 2006, **8**. DOI: 10.1039/b515623h.

8. A. V. Marenich, C. J. Cramer and D. G. Truhlar, *J. Phys. Chem. B*, 2009, **113**, 6378.

9. T. Lu and F. Chen, *J Comput. Chem.*, 2011, **33**, 580-592.

10. J. Zhang and T. Lu, *Phys. Chem. Chem. Phys.*, 2021, **23**, 20323-20328.

11. Kresse, G. and J. Furthmuller, *Phys. Rev. B* 1996. **54**, 11169-11186.

12. P. E. Blöchl, *Physical Review B*, 1994, **50**, 17953-17979.

13. ohn P. Perdew, K.B., and Matthias Ernzerhof, *Phys. Rev. Lett.*, 1996, **77**, 3865-3868.

14. Z. Yuan, Y. Duan, H. Zhang, X. Li, H. Zhang and I. Vankelecom, *Energy Environ. Sci.*, 2016, **9**, 441-447.

15. J. Wu, C. Yuan, T. Li, Z. Yuan, H. Zhang and X. Li, *J. Am. Chem. Soc.*, 2021, **143**, 13135-13144.

16. L. Zou, K. Shi, H. Liu, Y. Wu, T. Xu, Q. Wang, Z. Chen, Z. Yang, R. Song, J. Su and W. Zhang, *Chem. Eng. J.*, 2023, **465**, 142794.

17. M. M. Ikhsan, S. Abbas, X. H. Do, H. Y. Ha, K. Azizi and D. Henkensmeier, *Adv. Energy Mater.*, 2024, 2400139. DOI: 10.1002/aenm.202400139.

18. Y. Wang, T. Wang, D. Dong, J. Xie, Y. Guan, Y. Huang, J. Fan and Y.-C. Lu, *Matter*, 2022, **5**, 162-179.

19. N. Zhang, Y. Dong, M. Jia, X. Bian, Y. Wang, M. Qiu, J. Xu, Y. Liu, L. Jiao and F.

Cheng, *ACS Energy Lett.*, 2018, **3**, 1366-1372.

20. J. Kim, K. Park, M. Kim, H. Lee, J. Choi, H. B. Park, H. Kim, J. Jang, Y. H. Kim, T. Song and U. Paik, *Adv. Energy Mater.*, 2024, **14**, 2303455.

21. W. Zhong, Z. Shen, J. Mao, S. Zhang, H. Cheng, Y. Kim and Y. Lu, *Energy Environ. Sci.*, 2024, **17**, 2059-2068.

22. R. Xue, Z. Wang, N. Yao, Y. Liu, H. Wang, M. Zhang, A. Shao, X. Tang, J. Liu, J. Tang, Z. Wang and Y. Ma, *Adv. Funct. Mater.*, 2024, **34**, 2400959.

23. M. Wu, C. Shi, J. Yang, Y. Zong, Y. Chen, Z. Ren, Y. Zhao, Z. Li, W. Zhang, L. Wang, X. Huang, W. Wen, X. Li, X. Ning, X. Ren and D. Zhu, *Adv. Mater.*, 2024, **36**, 2310434.

24. Y. Liu, Y. Sun, J. Zhang, X. Hao, M. Zhang, P. Wei, X. Zhao and K. Cai, *Nano Energy*, 2024, **120**, 109152.

25. D. Jia, Z. Shen, Y. Lv, Z. Chen, H. Li, Y. Yu, J. Qiu and X. He, *Adv. Funct. Mater.*, 2024, **34**, 2308319.

26. Y. H. Lee, Y. Jeoun, J. H. Kim, J. Shim, K. S. Ahn, S. H. Yu and Y. E. Sung, *Adv. Funct. Mater.*, 2024, **34**, 2310884.

27. C. Li, R. Kingsbury, A. S. Thind, A. Shyamsunder, T. T. Fister, R. F. Klie, K. A. Persson and L. F. Nazar, *Nat Commun*, 2023, **14**, 3067.

28. Y. Wang, Z. Wang, W. K. Pang, W. Lie, J. A. Yuwono, G. Liang, S. Liu, A. M. D. Angelo, J. Deng, Y. Fan, K. Davey, B. Li and Z. Guo, *Nat Commun*, 2023, **14**, 2720.

29. C. Wang, X. Zeng, J. Qu, J. M. Cairney, Q. Meng, P. J. Cullen and Z. Pei, *Matter*, 2023, **6**, 3993-4012.

30. X. Guo, J. Lu, M. Wang, A. Chen, H. Hong, Q. Li, J. Zhu, Y. Wang, S. Yang, Z. Huang, Y. Wang, Z. Pei and C. Zhi, *Chem*, 2024, **10**, 1-15. DOI: 10.1016/j.chempr.2024.07.028.

31. Y. Kim, Y. Park, M. Kim, J. Lee, K. J. Kim and J. W. Choi, *Nat Commun*, 2022, **13**, 2371.

32. W. Wang, X. Zhang, S. Wu, B. Xu, S. Li, L. He, X. Li, Z. Chen, Y. Fan and A. L. R. Vellaisamy, *J. Raman Spectrosc.*, 2020, **51**, 2182-2191.

33. Q. Zhang, J. Luan, L. Fu, S. Wu, Y. Tang, X. Ji and H. Wang, *Angew. Chem. Int. Ed.*, 2019, **58**, 15841-15847.

34. H. Wang, W. Wei, X. Liu, S. Xu, Y. Dong and R. He, *Energy Storage Mater.*, 2023, **55**, 597-605.

35. Y. Wang, L. Yang, P. Xu, L. Liu, S. Li, Y. Zhao, R. Qin and F. Pan, *Small*, 2024, **20**, 2307446.

36. C.-Y. Li, J.-L. Wang, D.-T. Zhang, M.-P. Li, H. Chen, W.-H. Yi, X.-Y. Ren, B. Liu, X.-F. Lu and M.-C. Liu, *J. Energy Chem.*, 2024, **97**, 342-351.

37. H. Li, Z. Liu, G. Liang, Y. Huang, Y. Huang, M. Zhu, Z. Pei, Q. Xue, Z. Tang, Y. Wang, B. Li and C. Zhi, *ACS Nano*, 2018, **12**, 3140-3148.